1990ApJ...353..549H

THE ASTROPHYSICAL JOURNAL, 353:549–563, 1990 April 20

HIGH-RESOLUTION 8–13 MICRON IMAGING OF THE PLANETARY NEBULAE BD +30°3639 AND NGC 6572

JOSEPH L. HORA,[1,2] LYNNE K. DEUTSCH,[1,3] WILLIAM F. HOFFMANN,[1,2] AND GIOVANNI G. FAZIO[1,3]
Received 1989 June 23; accepted 1989 October 18

ABSTRACT

We present high-resolution (0".78 pixel^{-1}) mid-infrared images of the planetary nebulae BD +30°3639 and NGC 6572 at 8.3, 8.7, 9.8, 11.2, and 12.4 μm, obtained with a 16 × 16 pixel array camera. These filters sample unidentified infrared (UIR) emission features and continuum radiation in the 8–13 μm spectrum. Analysis of the maps of BD +30°3639 supports a model in which the infrared emission originates from two spatially distinct components, one which is responsible for the continuum radiation at 8–12 μm and the other which produces the emission-line features. The NGC 6572 images provides evidence for a previously undetected 11.2 μm UIR emission feature. Comparison with radio continuum maps indicates that the distribution of dust is similar to the distribution of ionized gas in each nebula. These results are compared to our previous observations of the planetary nebula NGC 7027 (Arens *et al.*; Tresch-Fienberg *et al.*). The spatial distribution of emission in these nebulae was found to be consistent with a model in which a single molecule or family of molecules, located on the outer edge of the continuum emission region, is responsible for the UIR emission.

Various models of source morphology are also investigated. The planetary nebulae BD +30°3639 and NGC 6572 can be modeled by an optically thin cylinder or a prolate ellipsoid with enhanced equatorial emission. These models reproduce well the general features of the nebula, such as the bipolar lobes of emission and the ring structure.

Subject headings: infrared: spectra — nebulae: individual (BD +30°3639, NGC 6572) — nebulae: planetary

I. INTRODUCTION

There are typically two components of the IR emission from dust in planetary nebulae: continuum emission due to a hot (≈230 K) core component, which is usually associated with the optical and radio nebula structure, and a cool (≈80 K) halo which is much more extended than the hot core component. In addition, the 2–14 μm infrared emission exhibits several unidentified infrared (hereafter UIR) emission features, at 3.3, 6.2, 7.7, 8.6, and 11.3 μm, observed in some planetary nebulae and many other objects. Since their initial detection, many materials and emission mechanisms have been proposed to explain the observed features (see reviews by Willner 1982; Puget and Leger 1989), but there is still no agreement on the identity of the carriers of these emission features. Many of these models require a particular spatial relationship between the feature emission in the different bands, the 10 μm continuum radiation, and the source of UV radiation. High-resolution imaging of these objects in the UIR bands can provide important information on the spatial distribution of the emission and help evaluate the proposed models.

The variety of observed planetary nebulae shapes and structures has made it difficult to derive a simple model that accounts for all observed forms. A spherical shell of material is an obvious choice for simple, highly symmetric nebulae, but even in the well-known Ring Nebula (NGC 6720), it was recognized early that the observed limb brightening is too large for such a model (Curtis 1918). Other possible structures that have been proposed are toroidal, cylindrical, and ellipsoidal shells (Khromov and Kohoutek 1968; Phillips and Reay 1977; Atherton *et al.* 1978; Balick 1987; Masson 1990). High-resolution imaging of planetary nebulae will help distinguish between these different models.

We have imaged the planetary nebulae BD +30°3639 and NGC 6572 at five discrete mid-infrared wavelengths with 0".78 pixel^{-1} resolution. We have previously obtained maps of NGC 7027 at the same resolution (Arens *et al.* 1984; Tresch-Fienberg *et al.* 1987). These three bright IR nebulae are members of the same morphological class, each having two symmetrical lobes of emission on an elliptical ring, with a central minimum. The planetary nebulae BD +30°3639 and NGC 7027 are both carbon-rich (C/O > 1) and exhibit several of the broad emission features at 7.7, 8.6, and 11.3 μm, along with various recombination and atomic fine structure lines (Fig. 1). The emission features are superposed on a continuum that peaks near 10 μm. The planetary nebulae NGC 6572 is not as carbon-rich as BD +30°3639 (C/O ≈ 1) and has much weaker UIR feature emission. In this paper, we present images of these three planetary nebulae and discuss their implications regarding the proposed models for UIR emission and source structure.

II. OBSERVATIONS AND DATA REDUCTION

The planetary nebula BD +30°3639 was observed with the NASA/GSFC IR array camera system on 1987 June 16 and 17 at the NASA IRTF on Mauna Kea. NGC 6572 was observed at the IRTF on 1988 May 22–24. The camera and data acquisition system have been described previously (Arens, Lamb, and Peck 1981, 1983; Lamb *et al.* 1983, 1984; Hoffmann *et al.* 1987). Images were taken at five discrete wavelengths, using mid-infrared bandpass filters with effective wavelengths (bandpasses) of 8.34(0.79), 8.75(0.88), 9.78(0.96), 11.19(0.57), and 12.36(0.27) μm. Our filter wavelengths and bandpasses sample the spectral features in the 8–13 μm range. For objects exhibiting emission lines in this range, the filters sample either

---

[1] Visiting Astronomer at the Infrared Telescope Facility, operated by the University of Hawaii under contract from the National Aeronautics and Space Administration.
[2] Steward Observatory, University of Arizona.
[3] Harvard-Smithsonian Center for Astrophysics.

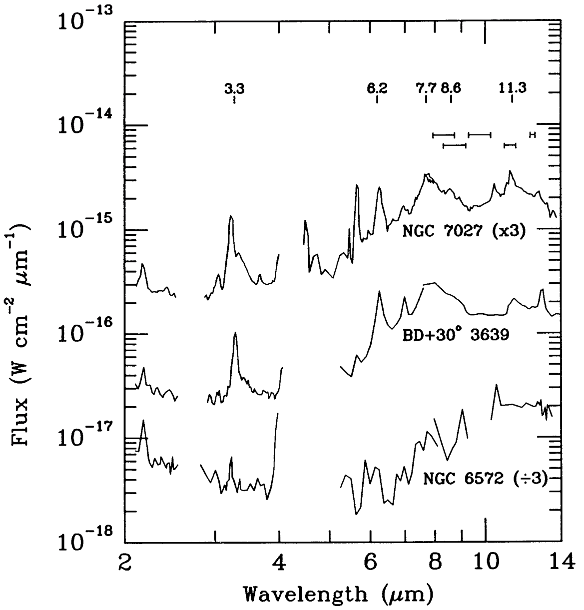

FIG. 1.—2–14 μm spectra of NGC 6572, BD +30°3639, and NGC 7027. The wavelengths of the UIR emission features are labeled at the top of the figure, in μm. The bandpass of the filters used in the observations presented in this paper are shown above the spectra. From left to right, they are the 8.3, 8.7, 9.8, 11.2, and 12.4 μm filters. The NGC 7027 data are from Merrill, Soifer, and Russell (1975) (2–4 μm), and Russell, Soifer, and Willner (1977) (5–14 μm). The BD +30°3639 data are from Russell, Soifer, and Merrill (1977) (2–4 μm), Cohen *et al.* 1986 (5–8 μm), and the IRAS LRS spectrum (Olnon and Raimond 1986; 7–14 μm). The NGC 6572 data are from Willner *et al.* 1979 (2–4 μm, 8–14 μm), and Cohen *et al.* 1986 (5–8 μm).

the continuum or feature emission. The 8.3 μm filter samples the long-wavelength half of the 7.7 μm emission feature, overlapping slightly the 8.6 μm feature. The 8.7 μm filter samples the 8.6 μm emission feature, including some of the radiation from the long-wavelength wing of the 7.7 μm emission line. The 9.8 μm filter samples the continuum region between the 8.6 and 11.3 μm emission lines. The 11.2 μm filter samples the 11.3 emission feature, and the 12.4 μm filter samples the emission plateau in the 11–13 μm spectral region. This emission plateau, which has been observed in many objects, is possibly emission from SiC, or polycyclic aromatic hydrocarbons (PAHs) or other large molecules. For objects that have silicate absorption and little or no spectral emission features, the 9.8 μm filter samples emission in the 9.7 μm silicate absorption "trough," and the 8.3 and 12.4 μm filters sample the continuum emission on both sides of the silicate feature.

The plate scale at the detector is 0".78 per pixel, making the size of the array 12".5 × 12".5. The diffraction-limited FWHM instrumental profile of a point source ranges from 0".9 to 1".1 between 8.3 and 12.4 μm. The observed FWHM size of point source images were 1".5 in right ascension and 2".7 in declination at all wavelengths. This size was due to the effects of seeing, errors in image registration, and charge spreading on the array in the declination direction. The rms noise in a single integration was estimated from observations of blank sky at 11.2 μm to be 0.2 Jy arcsec^{-2} in a 30 second integration. For a point source detection, this would correspond to a noise equivalent flux density (NEFD) of 2 Jy.

The maps were constructed from a set (15–25) of individual 15 second on-source integrations at each wavelength. Beam switching (chopping) was 15" S at 1 Hz, and the telescope was nodded 25"W. The individual images were expanded by 4 in both R.A. and declination (each pixel was subdivided by four subpixels, making the image size 64 × 64 pixels), and registered to the nearest $\frac{1}{4}$ (0".2) pixel using offsets recorded at the telescope. The images were then coadded and averaged to produce the maps. The position of the source on the array was continually referenced to the optical source to eliminate any errors due to telescope drift. The validity of the offsets was confirmed by calculating relative offsets between the individual integrations using a spatial cross-correlation algorithm (Barnea and Silverman 1972; Tresch-Fienberg *et al.* 1987). These differed from our recorded offsets by less than an instrumental pixel. The offset from the optical center of the nebula was changed by approximately 0".4 between every integration taken, so that the nebula was observed at different positions on the array, and to satisfy the Nyquist sampling criterion. The entire IR-emitting region was contained on the array in each individual integration. Image registration errors are estimated to be ±0".5, or less than 1 instrumental pixel.

Images were corrected for pixel-to-pixel variations in sensitivity using flat-field correction matrices obtained from observations of blank sky at two different air masses at the beginning of each night. Absolute flux calibration and air-mass correction were done by observing IR standard stars (μ Cep, α Sco, and γ Dra) immediately before and after each set of nebula observations with the same chopper throw and integration times. The errors in flux given in each bandpass include errors in the standard star observations as well as in the planetary nebulae.

After constructing the images of BD +30°3639 and the standard stars, the maps were deconvolved using the maximum entropy system MEIRS (Weir 1987). This is an image restoration system that is based on the maximum entropy routines MEMSYS II developed by Skilling and Bryan (1984). The point source function used for the array was the image of the standard star taken at the same wavelength immediately preceding the observations of the object. In each image reconstruction, the maximum entropy restoration converged quickly and monotonically to the final map. A reconstructed point source (α Her) is shown in Figure 2. This reconstructed MEIRS "beam" is elliptical, with FWHM sizes of 0".41 in the E-W direction and 0".75 in the N-S direction.

The intensity maps of BD +30°3639 and NGC 6572 presented here are maximum entropy restorations of the data. The source size and peak separation measurements were performed on these maps. The ratio, "feature," and temperature maps of BD +30°3639, NGC 6572, and NGC 7027 presented here were calculated from the unreconstructed data maps.

III. RESULTS AND DISCUSSION

a) BD +30°3639

Calibrated contour maps of BD +30°3639 at five wavelengths are shown in Figure 2. The lowest contour level and level spacing of each map was chosen to be 5 times the pixel-to-pixel rms in the background of the unreconstructed data map. All the maps exhibit the predominant features of an almost circular shape and double-peaked structure with a central minimum. Our maps resemble the lower resolution (3".4 beam) maximum entropy images produced by Bentley *et al.* (1984), whose infrared maps at 8.7 and 11.4 μm also showed a double-lobed structure, with an object FWHM size similar to ours. However, our images show other features not resolved in

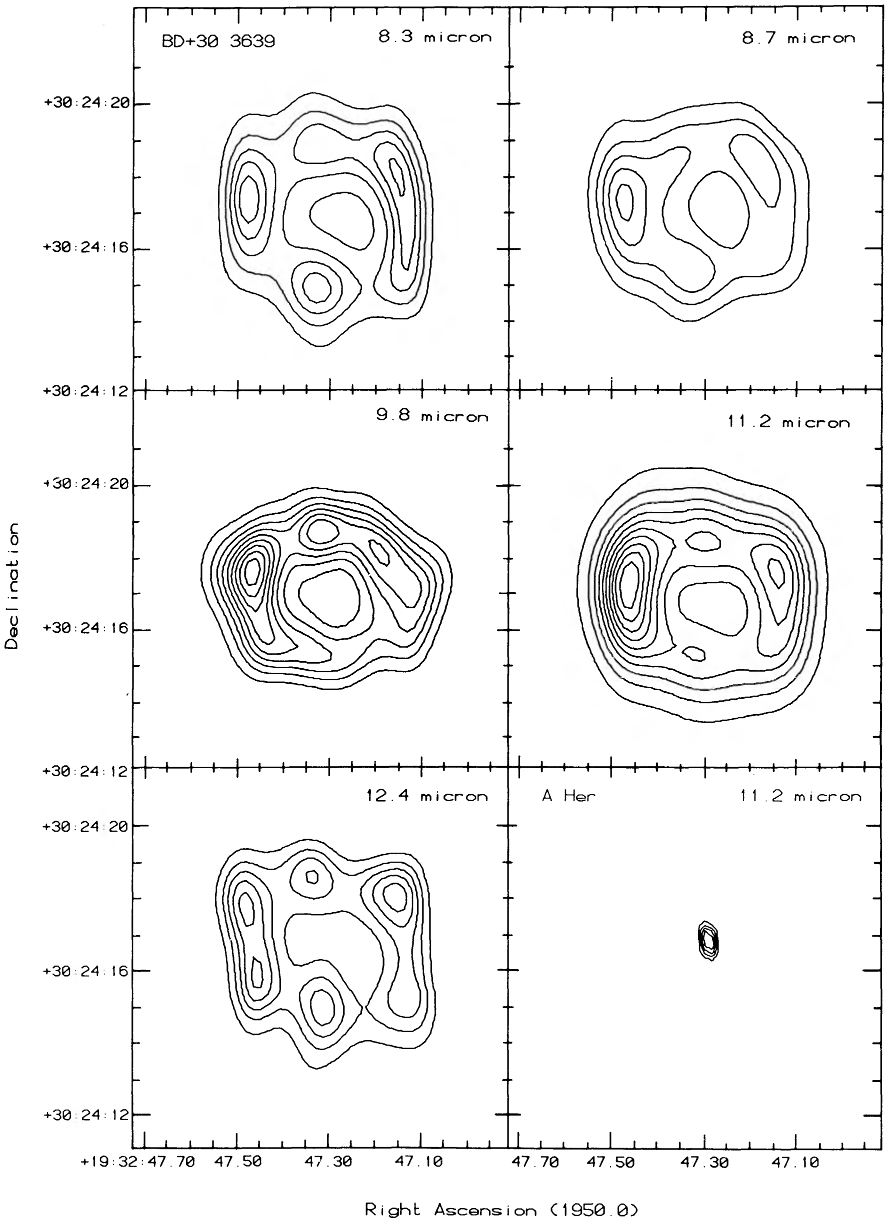

FIG. 2.—Contour maps of BD +30°3639. Contour levels are evenly spaced, with the lowest level equal to 5 σ of the unreconstructed data map. 8.3 μm map: $\lambda = 8.34$ μm, $\Delta\lambda = 0.79$ μm. Contour level spacing = 0.41 Jy arcsec^{-2}. 8.7 μm map: $\lambda = 8.75$ μm, $\Delta\lambda = 0.88$ μm. Contour level spacing = 0.45 Jy arcsec^{-2}. 9.8 μm map: $\lambda = 9.78$ μm, $\Delta\lambda = 0.96$ μm. Contour level spacing = 0.40 Jy arcsec^{-2}. 11.2 μm map: $\lambda = 11.19$ μm, $\Delta\lambda = 0.57$ μm. Contour level spacing = 0.44 Jy arcsec^{-2}. 12.4 μm map: $\lambda = 12.34$ μm. $\Delta\lambda = 0.27$ μm. Contour level spacing = 0.90 Jy arcsec^{-2}. A Her map: this is an 11.2 μm image of α Her, which has been deconvolved with a different 11.2 μm image of α Her to show the resolution of the MEM process. The FWHM size of this image is 0".41 in the E-W direction, and 0".75 in the N-S direction.

these lower resolution maps, such as the separation of the lobes into distinct clumps of emission in several of the maps.

The total flux of BD +30°3639 in each observed band was estimated by taking the sum of the source pixels in the calibrated map. A comparison of these observations with previous photometric studies of BD +30°3639 is presented in Table 1. These measurements agree well with previous observations. Besides confirming the quality of the data, the correspondence of our measured fluxes with the large beam photometry indicates that our array is sampling most of the emission at these wavelengths, and that there is not a significant amount of emission that is extended beyond the 15" observed by the array.

i) *Spatial Distribution of the 8–13 Micron Radiation*

There are many differences between the emission at different wavelengths that can be seen by examining the maps in Figure 2. Besides the two main lobes located east and west of the central minimum, there are also lobes to the north and south of the central minimum. In the emission feature maps, the southern lobe is brighter than the northern lobe (8.3 and 12.4 μm maps) or about equal brightness (11.2 μm map). In the 9.8 μm continuum image, however, the northern lobe is much brighter than the southern lobe in that image, with the southern lobe almost not present.

TABLE 1

COMPARISON OF BD +30°3639 OBSERVATIONS TO PREVIOUS PHOTOMETRY

	F_ν (Jy)			
λ (μm)	These Observations	Bentley *et al.* 1984	Gillett, Merrill, and Stein 1972	Jameson *et al.* 1974
8.3....	44 ± 4	...	54[a]	...
8.7....	52 ± 4	45 ± 7	...	53.5[b]
9.8....	48 ± 5	...	...	...
11.2....	79 ± 7	78 ± 8	80 ± 8[c]	57.2[d]
12.4....	75 ± 10	...	...	88[e]

[a] $\Delta\lambda/\lambda = 0.2$.

[b] 8.6 μm, $\Delta\lambda = 0.8$ μm.

[c] 11.0 μm, $\Delta\lambda = 1.8$ μm.

[d] $\Delta\lambda = 2.0$ μm.

[e] $\Delta\lambda = 2.0$ μm.

TABLE 2

SIZES OF BD +30°3639

λ (μm)	E-W FWHM SIZE	N-S FWHM SIZE	DISTANCE BETWEEN PEAKS	
			(E-W)	(N-S)
8.3	5″.4	5″.7	4″.5	3″.9
8.7	5.2	5.0	4.0	3.3
11.2	5.4	5.3	4.3	3.3
12.4	5.4	5.3	4.1	3.5
9.8	5.5	4.5	4.4	3.3
2 cm[a]	5.5	4.5	4.6	3.7
6 cm[a]	5.8	5.0	4.5	3.6

[a] Masson 1989*b*.

The sizes of BD +30°3639 at each of the wavelengths are compared in Figures 3*a* and 3*b*. These figures show source profiles taken through the nebula in the E-W and S-N directions. The profiles have been normalized and offset by a constant value, and the left (east or south) peak has been aligned with the other profiles in the figure. The source sizes based on these profiles have been summarized in Table 2. The FWHM size is defined as the full width of the profile in Figure 3 at a normalized intensity of 0.5 (the values have been normalized so that the maximum intensity equals 1.0 in every profile). In the E-W direction (Fig. 3*a*), the nebula is very similar in size at all wavelengths, with a difference of 0″.3 between the largest and smallest FWHM size. In the S-N profiles, more differences between the images are apparent. The 9.8 μm continuum map has the smallest FWHM size and a small peak separation. The difference in source sizes between the 9.8 μm image and the images in the UIR bands suggests that the continuum emission region is spatially distinct from the region of line emission.

Ratio maps, shown in Figure 4, were constructed to compare the maps. The line emission maps (8.3, 8.7, and 11.2 μm maps) and the 12.4 μm map (which samples the emission plateau) are compared to the 9.8 μm continuum map, and also two of the line emission maps (8.3 and 11.2 μm) maps are compared with each other. The maps were normalized so the average value in the map is 1.0.

The line-to-continuum ratio maps are fairly constant across the inner 5″ of the nebula. The rms deviation of the flux ratio in this region of the nebula for all the ratio maps was 8%–12%. The largest deviation occurs near the NW and S edges of the nebula. In these regions the ratio increases to approximately 2, indicating that more emission is coming from the spectral features than from the continuum at these locations. In the line ratio map (Fig. 4, 11.2/8.3), however, there is no such increase at the edge of the nebula. This is a result of the smaller size of the continuum image in the N-S direction, as was seen in the source profiles presented in Figure 3*b*.

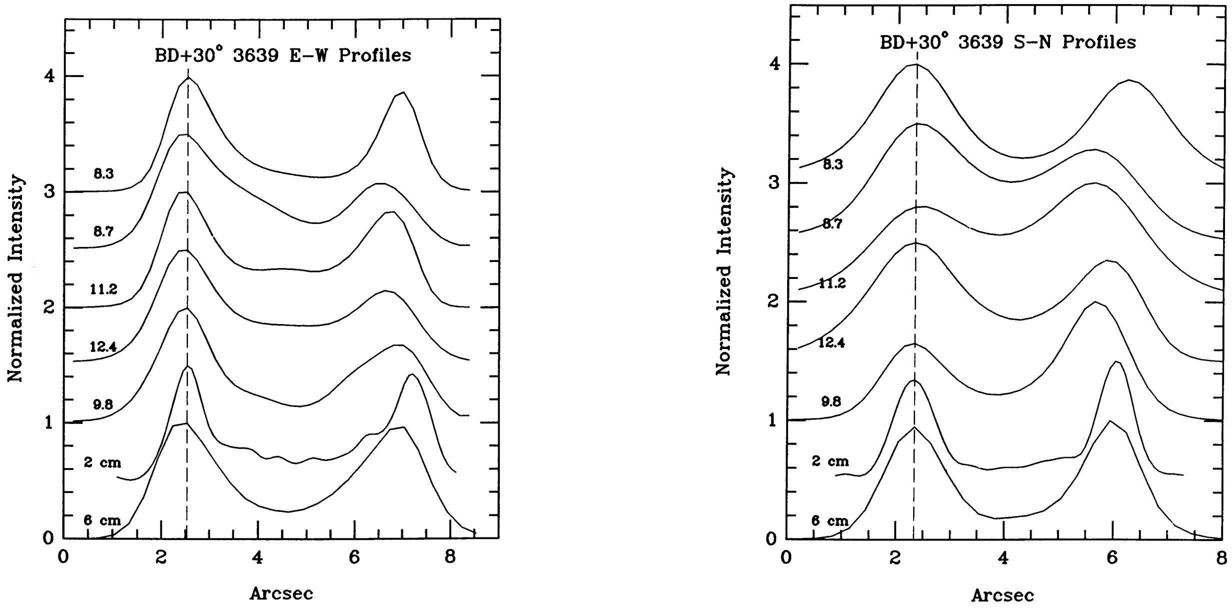

FIG. 3*a*

FIG. 3*b*

FIG. 3.—Source profiles of BD +30°3639. The profiles have been normalized and offset by a constant amount, and the left (east and south) peak has been aligned with the vertical dotted line to show the differences in the source sizes. (*a*) Source profiles in the east to west direction, at a declination of +30:24:17. The following offsets have been added to the normalized profiles: 8.3 μm: 3.0, 8.7 μm: 2.5, 11.2 μm: 2.0, 12.4 μm: 1.5, 9.8 μm: 1.0, 2 cm: 0.5, 6 cm: 0.0. (*b*) Source profiles in the south to north direction, at an R.A. of 19:32:47.3. The offsets uses are the same as in (*a*).

1990ApJ...353..549H

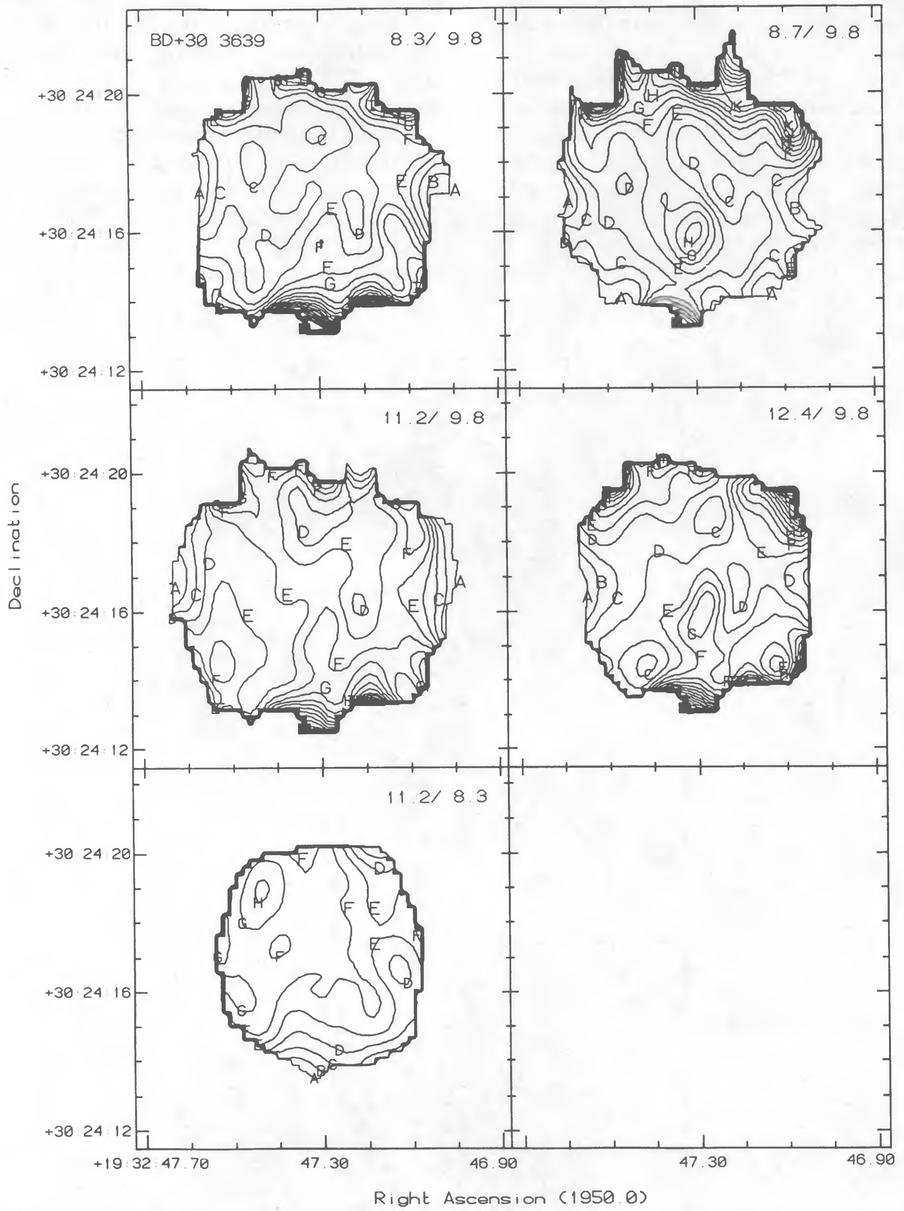

FIG. 4.—Dimensionless flux ratio contour maps of BD +30°3639, calculated from the data maps in each band. The ratio was calculated at all points where the signal-to-noise is greater than 3 in both images. Contour level spacing is 0.1, starting at level A = 0.6.

The continuum map also differs from the emission feature maps in that the central minimum is slightly to the south and deeper than in the line maps. This difference is evident as a local maximum in the ratio maps slightly below the center of the nebula. The positions of the intensity peaks in the continuum and line feature maps are also different, creating other local maxima and minima in the ratio maps.

These results agree with the study by Bentley *et al.* (1984), whose 8.7/10 μm and 11.4/10 μm maps also showed a difference in the spatial distribution of the line and continuum emission. However, our ratio maps differ from those of Bentley *et al.* in that the ranges of ratios in all the maps presented here are much smaller. The difference between our results and those of Bentley *et al.* may be a result of their continuum map which was used in the ratio calculation. Their broad-band ($\delta\lambda = 5.0$ μm) measurement of the continuum flux was contaminated by emission from the 7.7 and 11.2 μm features, so they subtracted properly scaled 8.7 and 11.4 μm maps from the 10 μm map to obtain a "continuum map." Our 9.8 μm measurement did not include any contamination from the UIR feature emission, so no special processing was necessary to obtain the continuum map.

ii) *Spectral Feature Maps*

The spatial distribution of the continuum and feature emission can also be compared by constructing "feature" maps at 8.3 and 11.2 μm by subtracting off the continuum flux at these wavelengths. It is clear from Figure 1 that a substantial amount of the flux at both 8.3 and 11.2 μm is due to the continuum emission. Therefore, if the continuum at the feature wavelengths is similar to the continuum at 9.8 μm, the difference between the 8.3 and 11.2 μm maps and the 9.8 μm map

1990ApJ...353..549H

should give maps that show exclusively emission in the 7.7 and 11.3 μm unidentified features.

Before the 9.8 μm map was subtracted, the intensity of the 9.8 μm map was scaled assuming a blackbody continuum emission at 250 K, which fit the continuum at 9.8 μm and continuum points outside of the 7.7 and 11.3 μm spectral features (see Fig. 1). The result of this calculation is shown in Figure 5. The lowest gray levels in these images are approximately 4 times the rms noise in the original data maps. A contour map of the 9.8 μm continuum emission is overlayed on the feature maps to show the spatial relationship between the feature and continuum emission. These gray-scale maps of $I_{8.3} - I_{8.3}^{\mathrm{continuum}}$ and $I_{11.2} - I_{11.2}^{\mathrm{continuum}}$ show a ring of emission with several intensity peaks located at the edge of the ring. In addition to the two major peaks at the E and W edges of the nebula as seen in the original data, there are peaks S of the central minimum and an extension of emission along the N edge of the nebula. These two "feature" maps, $I_{8.3} - I_{8.3}^{\mathrm{continuum}}$ and $I_{11.2} - I_{11.2}^{\mathrm{continuum}}$, each have peaks that are located in the same position around the ring of emission, again showing the

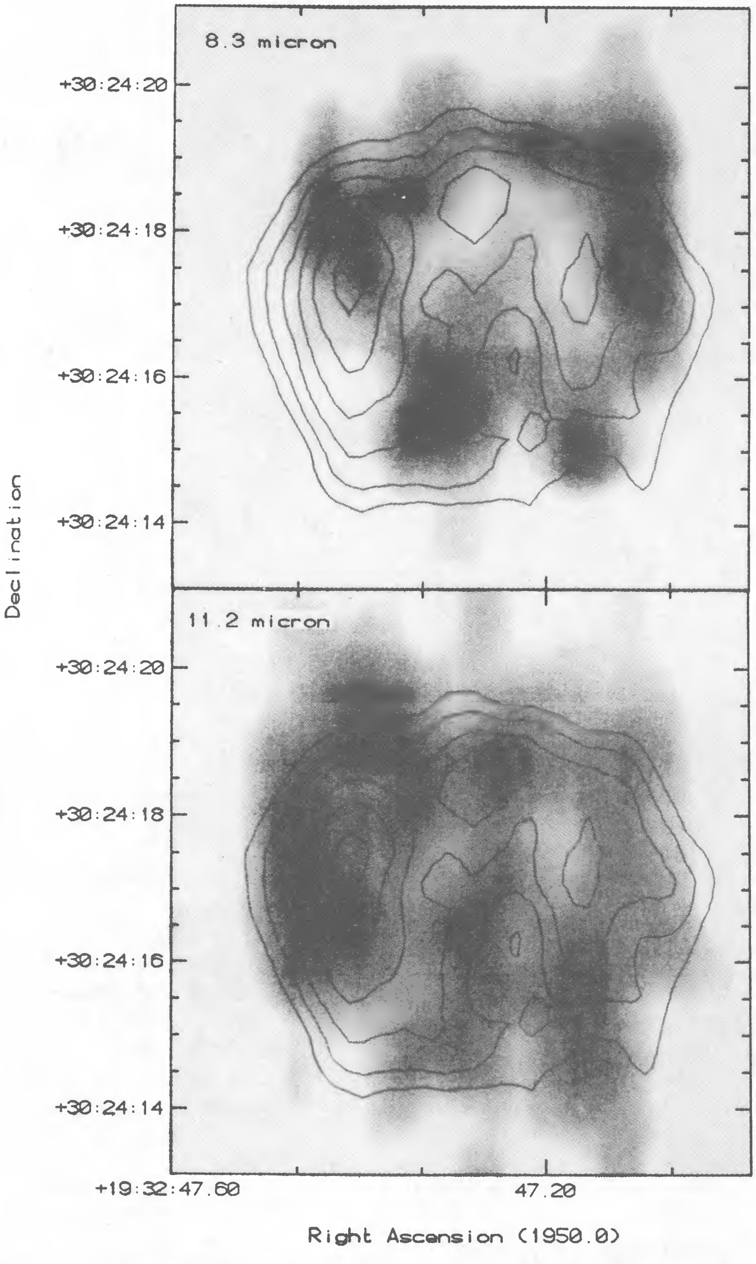

FIG. 5.—Gray-scale images of the continuum subtracted "feature" maps of BD +30°3639 at 8.3 and 11.2 μm. The 9.8 μm map has been superposed to show the relationship between the continuum and feature emission. The maps in this figure are the data maps without MEM reconstruction. Contour intervals for the 9.8 μm map are 0.16 Jy arcsec^{-2}, starting from the lowest level of 0.84 Jy arsec^{-2}, which is half the peak intensity. Both the 8.3 and 11.2 feature maps show peaks of emission around the periphery of the nebula, in roughly the same location. In the 8.3 μm feature map, the darkest gray-scale level corresponds to a value of 1.5 Jy arcsec^{-2}; the lightest level corresponds to a value of 0.5 Jy arcsec^{-2}. In the 11.2 μm feature map, the darkest gray-scale level corresponds to a value of 1.2 Jy arcsec^{-2}, and the lighest level corresponds to a value of 0.3 Jy arcsec^{-2}.

similarity between the spatial position of the 7.7 and 11.3 μm feature emission, and the different distribution of the continuum emission. The emission does differ, however, in that the 7.7 μm feature is strongest in the west lobe of the nebula, whereas the 11.3 μm feature peaks in the east lobe. This may be due to different conditions in these parts of the nebula, such as temperature, density, or radiation received, which could cause one emission feature to be stronger relative to the other.

b) *NGC 6572*

Calibrated contour maps of NGC 6572 are shown in Figure 6. The total fluxes for the nebula at the wavelength observed are given in Table 3. We detected the nebula at 8.3 μm, but there was insufficient time to completely map the nebula at that wavelength. This nebula also has the characteristic double-lobed structure similar to BD +30°3639 and NGC 7027. However, NGC 6572 is different from these two in that the observed UIR feature emission is relatively weak in this nebula (Fig. 1).

Table 4 gives the measured E-W FWHM source sizes and peak separations for the images presented here. The S-N source FWHM are not given here, since these profiles pass through the null line between the two lobes. There are significant differences in both the global and local spatial features among the maps at different wavelengths. Though all maps display the familiar double-lobed structure, the 9.8 μm map does not show the overall oval shape of the other maps. The two lobes of the 9.8 μm map approach convergence in the northern portion of the nebula, and the nebula has an extension of its western lobe to the southwest which is not seen in the other maps. The central minimum is much more pronounced in the 9.8 and 12.4 μm maps, and these two maps

TABLE 3

PHOTOMETRY OF NGC 6572

λ (μm)	F_ν (Jy)
8.7	10.0 ± 0.8
9.8	10.9 ± 1.0
11.2	21.4 ± 1.2
12.4	27.8 ± 2.3

TABLE 4

SIZES OF NGC 6572

λ (μm)	E-W FWHM Size	Distance Between Peaks (E-W)
8.7	5″.3	3″.8
9.8	5.2	3.4
11.2	5.4	3.5
12.4	5.4	3.8
2 cm[a]	5.2	3.7
6 cm[a]	5.5	3.4

[a] Masson 1989*b*.

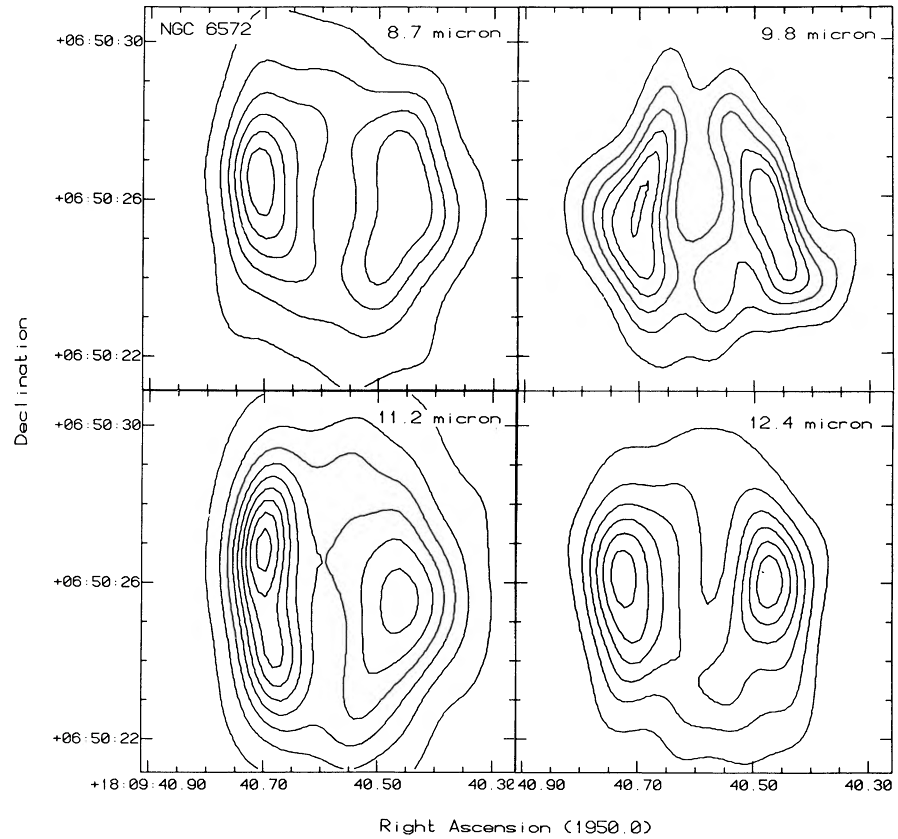

FIG. 6.—Contour maps of NGC 6572. Contour levels are evenly spaced, with the lowest level equal to 3 σ of the unreconstructed data map. 8.7 μm map: $\lambda = 8.75$ μm, $\Delta\lambda = 0.88$ μm. Contour level spacing = 0.063 Jy arcsec^{-2}. 9.8 μm map: $\lambda = 9.78$ μm, $\Delta\lambda = 0.96$ μm. Contour level spacing = 0.078 Jy arsec^{-2}. 11.2 μm map: $\lambda = 11.19$ μm, $\Delta\lambda = 0.57$ μm. Contour level spacing = 0.087 Jy arcsec^{-2}. 12.4 μm map: $\lambda = 12.34$ μm, $\Delta\lambda = 0.27$ μm. Contour level spacing = 0.186 Jy arcsec^{-2}.

show an additional peak southwest of the central minimum. The eastern lobe of the 11.2 μm map is greatly elongated toward the north with respect to its western lobe, producing a northeast-to-southwest asymmetry. The 8.7 μm map shows an asymmetry of similar orientation in its overall structure.

Emission from the lobes shows both intensity as well as spatial variations among all of the maps. The peak pixel intensity is much greater in the eastern lobe as compared to the western lobe in the 8.7 and 11.2 μm emission maps (by approximately 30%), while this peak intensity is the same in the two lobes for the 9.8 μm continuum and the 12.4 μm maps. When summing intensity values over approximately 50 subpixel regions centered on the peak of each lobe, all four maps show some enhanced emission in the eastern lobe, though the difference in flux for the 8.7 and 11.2 μm maps greatly exceeds that for the 9.8 and 12.4 μm maps. This suggests that more dust is present in the eastern lobe of NGC 6572. Also, the relative positions of the peaks in each lobe vary with wavelength. The eastern lobe of the 9.8 μm map peaks about 0″.5 south of the western lobe; at 8.7 and 12.4 μm, the peaks have about the same north-south position in both lobes; and at 11.2 μm, the western lobe peaks 1″.4 north of the eastern lobe.

The nebula NGC 6572 is much fainter than BD +30°3639 and our signal-to-noise was lower, so the ratio and feature maps are much noisier and are not presented here. Instead, the distribution of the emission at the continuum and feature wavelengths is compared in Figure 7, where the 11.2 μm map has been superposed on the 9.8 μm image. This figure clearly shows the displacement of the eastern 11.2 μm lobe to the north of the eastern 9.8 μm lobe. This effect does not seem to be due to a temperature gradient, since the 8.7, 9.8, and 12.4 images do not show any similar displacement of the lobe.

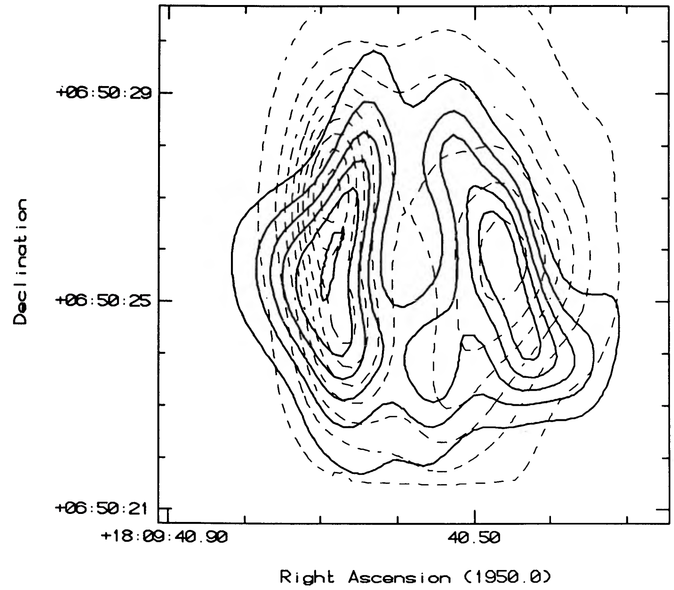

FIG. 7.—Contour map of NGC 6572 at 9.8 μm from Fig. 6, with the contour map at 11.2 μm from Fig. 6 superposed as the dotted contours. Note that the peak of the eastern lobe in the 11.2 μm image is located approximately 1″.5 to the north of the 9.8 μm lobe.

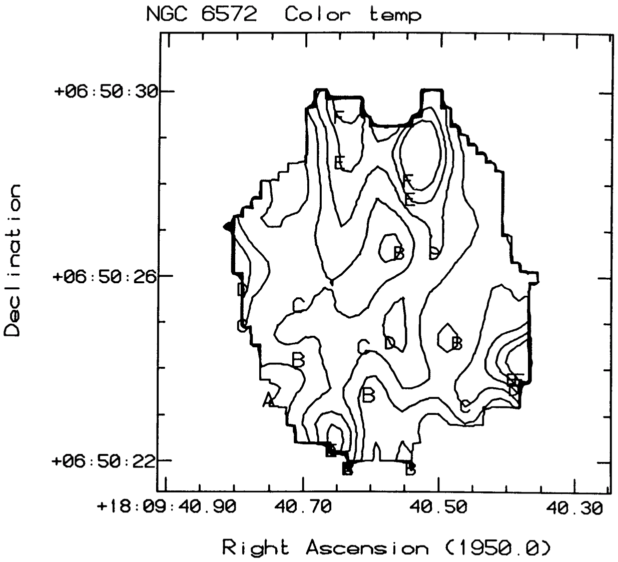

FIG. 8.—Color temperature map of NGC 6572, calculated from the 9.8 and 12.4 μm data maps. The temperature was calculated in all locations where the signal-to-noise was greater than 2 in both maps. The contour spacing is 15 K, starting from level A = 155 K. The temperature is roughly flat across the nebula, with an average temperature of 185 ± 12 K in the central 6″.

By assuming that the IR radiation at 9.8 and 12.4 μm is thermal emission from dust grains, we can calculate a color temperature map for the nebula. This calculation was performed in 4 × 4 subpixel bins (1 × 1 instrumental pixel) with a one subpixel step size (1/4 instrumental pixel step), and only for those regions where signal-to-noise is greater than 2 in both images. Expressing the intensity of emitted radiation in terms of a modified Planck law $Q_\lambda B_\lambda(T)$ per unit wavelength, where $Q_\lambda \propto \lambda^{-n}$ is the wavelength dependent emissivity of the grains, the color temperature T_c can be calculated from solving the following equation for T_c:

$$\frac{I_{12.4}}{I_{9.8}} = \frac{Q_{12.4}B_{12.4}(T_c)}{Q_{9.8}B_{9.8}(T_c)}\,.$$

The result for $n = 0$ is shown in Figure 8. Higher values for n, such as $n = 1$ or 1.5, lowers the absolute temperature by about 20 K, but the relative temperature distribution is unaffected. The average value of T_c in the central 6″ is 185 ± 12 K, where the uncertainty includes the uncertainty in the absolute calibration of the images in each of the wavelengths. The temperature is relatively constant over the entire nebula, with no large gradients or variations with radius. The standard deviation of 12 K over the central 6″ of the nebula is comparable to the uncertainty in temperature expected from noise in the 9.8 and 12.4 μm maps used in the temperature calculation. Therefore, the temperature variations seen in the map are not significant, and the temperature of the emitting grains is constant to this accuracy.

c) Comparison of NGC 7027, BD +30°3639, and NGC 6572

The nebula NGC 7027 is the brightest and most extensively observed planetary nebula at mid-infrared wavelengths. High-resolution observations have been made by Bentley (1982), Aitken and Roche (1983), and with this camera (Arens *et al.* 1984; Tresch-Fienberg *et al.* 1987). These studies all show the same double-lobed structure with central minimum, similar to BD +30°3639 and NGC 6572. The same UIR features are present in NGC 7027 as in BD +30°3639 (see Fig. 1).

The spatial distribution of feature emission at 7.7 and 11.3 μm in NGC 7027 is correlated, and the feature emission is spatially distinct from the continuum emission at 10 μm

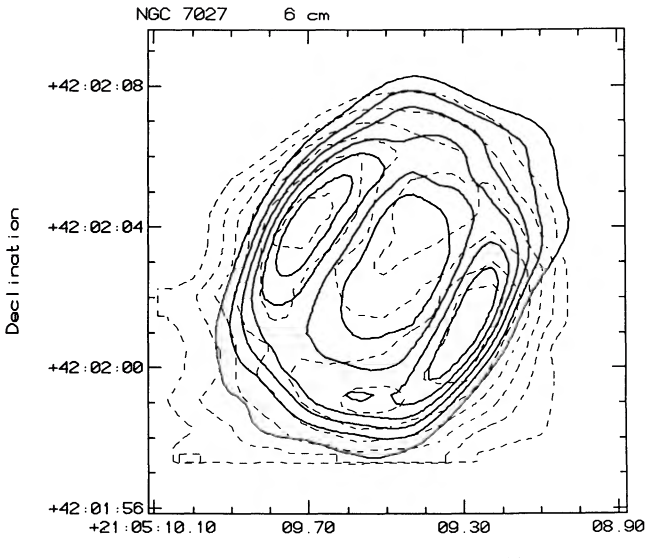

FIG. 9*a*

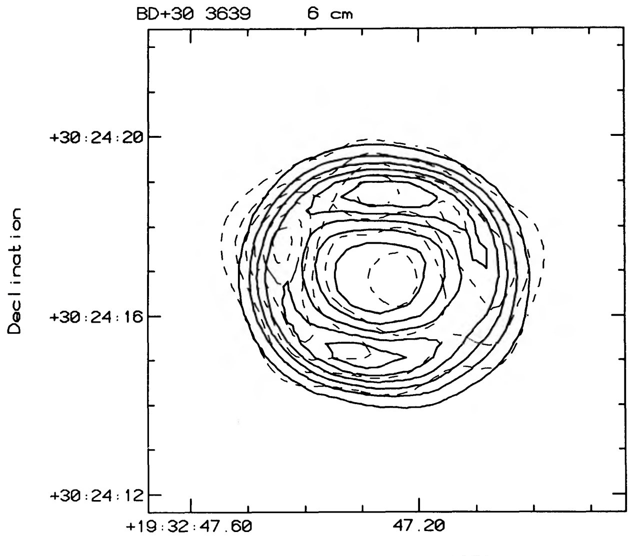

FIG. 9*b*

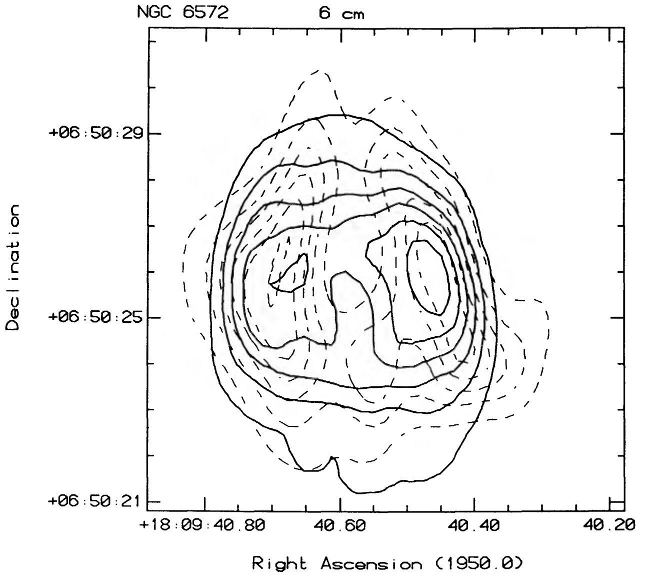

FIG. 9*c*

FIG. 9.—Radio continuum maps of the planetary nebulae, from Masson (1989*a*, *b*). The 9.8 μm continuum map has been superposed on the radio images as the dashed contours. (*a*) NGC 7027, 6 cm. Contour level spacing = 4.38×10^{-3} Jy beam^{-1}. (*b*) BD +30°3639, 6 cm. Contour level spacing = 1.92×10^{-3} Jy beam^{-1}. (*c*) NGC 6572, 6 cm. Contour level spacing = 2.36×10^{-3} Jy beam^{-1}.

(Bentley 1982; Aitken and Roche 1983; Tresch-Fienberg 1985). The feature emission regions were found to be slightly more extended than the continuum regions, although there is some disagreement on the feature emission size difference. The 3.3 μm feature emission has also been found to be more extended than the ionized gas emission, with the 3.3 and 3.4 μm features having a similar spatial distribution (Woodward *et al.* 1987).

The continuum-subtracted feature maps of BD +30°3639 described above (Fig. 5) show that the feature emission regions are located in a ring of emission around the central minimum. A similar result was found for NGC 7027. Tresch-Fienberg (1985) found that the 11.2 μm feature emission was located in a ring symmetrically located around the central minimum of emission. The 11.2 μm feature map showed additional differences between the feature and continuum emission, with a shift in the location of the central minimum and a difference in relative peak intensity of the two main lobes of emission. On the other hand, the difference map between the 11.2 and 9.8 μm maps for NGC 6572 shows no ring of emission.

In all three of the nebulae NGC 7027, NGC 6572, and BD +30°3639, the emission in the continuum bands is spatially distinct from the emission in the wavelengths of UIR emission. The overall size and shape appearance of the nebulae are similar, but the nebulae appear to be slightly more spatially extended at the UIR wavelengths. Also, the additional radiation seen in the UIR bands is emitted primarily from one or more of the bright lobes of the nebula, and these peaks of emission appear to be located in different locations than the emission peaks in the continuum regions of the spectrum.

d) *Comparison of IR and Radio Maps*

There is also a close correspondence between the infrared and radio continuum structure of these planetary nebulae (Basart and Daub 1987; Terzian 1987; Masson 1989*a*, *b*). Radio maps of the nebulae at a similar resolution to the IR maps are reproduced in Figures 9*a*–9*c* from Masson (1989*a*, *b*). These VLA CLEAN maps of NGC 7027, BD +30°3639, and NGC 6572 have Gaussian beam FWHM sizes of 1″.05, 0″.96, and 1″.06, respectively. The 9.8 μm map for each nebula have been plotted as dotted contours over the 6 cm radio map. The radio maps of these nebulae are similar in general appearance to the IR emission maps, having a double-lobed structure with central minimum that is usually aligned with the IR lobes. They are not only similar in general appearance, but in detail also. In NGC 7027, the southern tip of the western lobe is resolved into separate knots of emission. These are located in the same position in both the radio and infrared maps. This provides evidence that the gas and dust are well mixed (Arens *et al.* 1984; Tresch-Fienberg 1985). As shown earlier, however, the feature emission is more spatially extended than the IR continuum at 10 μm. Therefore, we conclude that the IR emission region is located on the outer edge of the ionized region producing the radio and the IR continuum emission.

In general, the radio images of BD +30°3639 by Basart and Daub (1987), Terzian (1987) and Masson (1989*b*) are similar to the IR emission, both having a near circular shape and similar size. The 2 and 6 cm maps (Masson 1989*b*) have FWHM sizes which are very similar to the sizes of the infrared images (Table 2). An interesting difference, however, is that the brightest lobes of radio emission are located on the N and S edges of the nebula, whereas in the infrared, the brightest emission seems to be aligned E-W. This effect was first seen in the lower resolution maps of Bentley *et al.* (1984), whose IR maps show the major peaks in the same positions on the nebula as the new data presented here. However, it should be noted that the radio emission peaks are a small feature on the main structure of a ring of emission. This ring is very similar in shape and size to that seen in our infrared images, and is slightly larger in the E-W direction than the N-S, as in the infrared images. The ring structure is most evident in the 9.8 μm continuum map, whereas the feature emission maps are much more intense in the lobes of emission on the outer edge of the ring structure.

The radio maps of NGC 6572 (Basart and Daub 1987; Terzian 1987; Masson 1989*b*) are also very similar to the infrared maps presented here. The FWHM size of the radio emission region is again very similar to the infrared source size, and the emission peaks are located in similar positions in the nebula (Table 4). There are considerable differences in the detailed IR and radio structure, however. In the radio maps at 2 and 6 cm (Masson 1989*b*, see Fig. 9), the west lobe is located slightly to the north of the east lobe, whereas in the IR maps presented here, either the lobes are aligned E-W, or the east lobe is slightly north. The relative intensity of the lobes is also different. In the radio maps, the west lobe is brighter. However, in the IR maps, the lobes are either of equal intensity or the east lobe is brighter. Also, there is a "bridge" of emission between the two radio lobes north of the nebula's central minimum. Where there is a connection in the IR lobes, this is present south of the central minimum.

In these three nebulae, the radio structure appears very similar to the observed infrared structure, which suggests that the gas and dust are generally coextensive. The correspondence between radio continuum and mid-IR structure is strongest in NGC 7027 and NGC 6572, where the bright lobes of emission are similar in position and extent. The different relative intensities of the peaks and minima of emission may be due to different gas to dust ratios in these regions. The nebula showing the largest discrepancy is BD +30°3639, where although the ring of emission is similar in size, the 10 μm and radio emission peaks are rotated 90° from each other. The fact that the radio size is slightly smaller than the infrared source size in some of these nebulae does not contradict the other evidence that the gas and dust are well mixed, as pointed out by Bentley (1982). The radio emission should be proportional to N_e^2, the square of the electron density in the nebula. However, if the gas and dust are well mixed, the infrared emission will be proportional to the gas density and therefore should be correlated with N_e. This difference in dependence on N_e would cause the observed radio emission to fall off more sharply than the infrared emission, as N_e decreases from the center of the nebula. Bentley *et al.* (1984) calculated models including this effect for BD +30°3639 and have shown that if the gas and dust are well mixed, the FWHM source size of the radio and infrared sources could differ by $1\overset{''}{.}5$–2″. The possibility still exists that the IR-emitting region lies just outside the ionized region, below the resolution limit of these observations. However, the data available to date are consistent with the dust and gas being coextensive but perhaps not well mixed (e.g., in BD +30°3639), and there is no evidence of significant mid-IR dust emission completely outside the ionized zone, as defined by the radio continuum emission.

e) Molecules as a Source of Spectral Features

Broad emission features have been observed at 3.3, 6.2, 7.7, 8.6, and 11.3 μm in the spectra of a wide variety of objects (see reviews by Aitken 1981; Willner 1982; Puget and Leger 1989), where all five bands are seen together in most objects. Since the discovery of these UIR bands, several possible models for this emission have been proposed. One is that simple molecules or radicals frozen in grain mantles could be excited and emit through their vibrational modes (Allamandola, Greenberg, and Norman 1979). Another model proposes the UIR bands are emitted by radicals bound at the periphery of graphitic grains (Duley and Williams 1981). A third possibility is that the emission originates from large carbon molecules, such as polycyclic aromatic hydrocarbons (PAHs) (Leger and Puget 1984), hydrogenated amorphous carbons (HACs) (Duley 1985), or quenched carbonaceous composites (QCCs) (Sakata *et al.* 1987). PAH molecules are promising candidates, because emission in these bands is characteristic of many large compact PAH molecules. A mixture of these molecules at different emission temperatures could account for the observed spectra.

If PAHs are the carriers of the UIR features, the observed emission might be attributed to IR fluorescence from UV-pumped, vibrationally and electronically excited PAHs (Allamandola, Tielens, and Barker 1985; d'Hendecourt and Leger 1987). Correlations have been found between the intensities of several pairs of UIR bands, such as the 3.3 and 11.3 μm bands (Duley and Williams 1981; Martin 1987) and the 6.2 and 7.7 μm bands (Cohen *et al.* 1986), and Cohen *et al.* found good correlations between the strengths of all bands. The measured laboratory spectrum for a PAH molecule demonstrates a strong temperature dependence in the relative strengths of the bands in the 3 and 11 μm regions (d'Hendercourt and Leger 1987).

UIR band intensities are also seen to depend on nebular C/O ratio in PNs (Cohen *et al.*, 1986; Martin 1987). For $C/O \approx 1$, observed UIR feature emission is weak, while a broad emission plateau from approximately 10.5–12.5 μm is seen (Pottasch 1987; Roche 1987; Barlow 1983). For a C/O ratio just greater than 1, most of the excess carbon will combine with silicon to form SiC, which condenses before graphite (Gilman 1969), and the observed 11–13 μm emission plateau is attributed to resonance in silicate carbide grains. The contribution of SiC emission to the observed spectra of PNs has been studied by Aitken and Roche (1982). Barlow (1983) found that 11–13 μm SiC emission correlated well with 3.3 μm UIR emission, but the 11.3 μm feature emission was always weak in PNs with strong SiC emission. For $C/O \gg 1$, the UIR emission features are strong in all five UIR bands.

Both BD +30°3639 and NGC 7027 are very carbon-rich, with C/O ratios of 2.8 and 3.5, respectively (Torres-Piembert and Pena 1981; Shields 1978). These nebulae show strong emission in the UIR feature bands and also exhibit the 11–13 μm plateau. It has recently been suggested by Witteborn *et al.* (1989) that the 11–13 μm plateau observed in these two objects may include emission from PAH clusters and amorphous carbon particles, while the discrete UIR bands arise from free molecular PAHs. The spectrum of planetary nebula NGC 6572, with C/O ≈ 1.1 (Seaton 1983), shows the broad emission plateau from 11–13 μm and only a subset of the IUR bands with relatively weak emission detected (Willner *et al.* 1979). Feature emission at 3.3 and 7.7 μm in NGC 6572 has been confirmed, with possible detections at 3.4 and 6.2 μm (Willner *et al.* 1979; Cohen *et al.* 1986; Martin 1987) and no detection of the 8.6 or 11.3 μm features.

The spatial distribution of the emitting grains in the 11.2 and 12.4 μm maps of NGC 6572 are expected to be similar if the emission is predominantly from SiC. Instead, the 11.2 μm map shows distinct differences with respect to the 12.4 μm map in both intensity and spatial distribution of the emission. At 11.2 μm, we see more intense emission from the eastern lobe, which peaks significantly further north than the eastern lobe of the 12.4 μm map. The central minimum is also more pronounced at 12.4 μm. In constrast with the 11.2 μm map, the 9.8 μm emission, which falls outside the SiC plateau and the feature emission bands, shows intensity and spatial distribution in the lobes which is quite similar to that seen at 12.4 μm—the lobes of each map are approximately symmetric in both intensity and relative position and the central minima are more pronounced than that in the 11.2 μm map. Finally, the 8.7 μm map bears more resemblance to the 11.2 μm map than to the other two maps in the greater intensity of its eastern lobe and its northeast-to-southwest asymmetry. Thus, it appears that the spatial distribution of the 12.4 μm emission resembles that of the continuum emission and is distinctly different than the 11.2 μm distribution.

One possible explanation of the observed morphologies is that the spatially distinct, higher intensity peak in the 11.2 μm image could be accounted for by a size distribution of SiC grains. Theoretical calculations predict a particle size for SiC in the atmospheres of carbon stars on the order of 0.1 μm (Friedemann 1969; Gilra 1973). Gilra (1972, 1973) has found that it is not the size but rather the *shape* of the particles which is the most important parameter in determining the wavelength dependence of the SiC emission. The emission process is one of collective excitations (Gilra 1972; Treffers and Cohen 1974). For a single shape of SiC particles, the emission spectrum should show a set of relatively narrow bands which would be shifted in frequency between 10.3 and 12.6 μm, depending on the oblateness or protateness of the shape. A distribution of shapes in a single IR source would produce a broad feature or emission plateau in the spectrum of that source between the fundamental frequencies. This plateau corresponds to the observed plateaus in the spectra of carbon stars such as IRC +10216 (Treffers and Cohen 1974) and planetary nebulae such as NGC 6572. If it is the shape of the SiC particles which determines the wavelength dependence of the emitted spectrum between 10 and 13 μm, then it is difficult to construct a scenario for the formation of SiC particles of one particular shape with a spatial distribution which is distinct from the fairly symmetric distribution of the majority of emitting SiC particles at 11.2 μm in NGC 6572. Furthermore, the similar intensity and spatial distribution of the peak emission in the eastern lobe of the 8.7 μm map as compared to that in the 11.2 μm map cannot be explained by SiC emission, because there is no such emission sampled within the 8.7 μm band. Therefore, it does not seem possible to attribute all the observed emission in the 11.2 μm map to SiC emission.

The C/O ratio of 1.1 for NGC 6572 suggests that the UIR emission should be much weaker than that seen in BD +30°3639 and NGC 7027, and this expected relationship is confirmed for the band strengths which have been observed in all three objects. Since the additional flux contribution from the eastern lobe in the 8.7 and 11.2 μm maps is on the order of only a few percent of the total flux from the object, this additional emission does not significantly alter the observed spectrum of the entire object and is only detected by its spatial distinctness. Thus, we conclude that 11.3 μm feature emission is seen in NGC 6572, and its spatial and intensity distribution supports the model in which the observed UIR band emission from carbon-rich planetary nebulae originates from a grain population which is distinct from the grain populations that produce the continuum and SiC emission. Our maps also provide some evidence for the presence of 8.6 μm UIR feature emission in NGC 6572.

f) PAH Temperature Map for NGC 7027

Assuming that the feature emission is due to PAH molecules, we can determine the average temperature $\langle T\rangle$ of the emitting molecule implied from the PAH model from the observed intensity of the 11.3 to 3.3 μm emission by solving the following equation for $\langle T\rangle$ (de Muzion, d'Hendecourt, and Gaballe 1987):

$$\frac{I_{11.3\,\mu\mathrm{m}}}{I_{3.3\,\mu\mathrm{m}}} = \frac{B_{11.3\,\mu\mathrm{m}}(T)}{B_{3.3\,\mu\mathrm{m}}(T)}\,\frac{A_{11.3\,\mu\mathrm{m}}}{A_{3.3\,\mu\mathrm{m}}}\,,$$

where A_λ is the infrared cross section of the band per C-atom. The intensity ratio $I_{11.3}/I_{3.3}$ has been calculated previously for a number of objects using broad beam measurements from various sources (deMuzion, d'Hendecourt, and Geballe 1987; Cohen *et al.* 1986).

With maps showing the spatial distribution of the emission, we can determine the temperature at different points across the nebula. This calculation was performed for NGC 7027 with the 11.2 μm map from Tresch-Fienberg (1985) and the 3.3 μm data from Woodward (1988). The 11.2 μm data were taken with this camera, and the 3.3 μm image was taken using an array with 1″.0 per pixel, similar to our 0″.78 per pixel. A cross section ratio $A_{11.2\,\mu\mathrm{m}}/A_{3.3\,\mu\mathrm{m}}$ of 10 was used for this calculation (Leger, d'Hendecourt, and Defourneau 1989). The result of this calculation is shown in Figure 10. The temperatures range from 670 to 870 K, with an average temperature of 755 ± 46 K in the 10″ diameter nebula. These temperatures are similar to those found for a wide range of objects with UIR feature emission (deMuizon, d'Hendecourt, and Geballe 1987). The average 11.2/3.3 μm intensity ratio in the central 10″ is 15 ± 4, higher than the value of 5.3 found by Bregman *et al.* (1983). This discrepancy may be due to our observations only including the central regions of the nebula. The intensity ratio decreases outside the 10″ ring of emission, to approximately 9 in the region just outside the ring covered by our array. Contribution to the 3.3 μm flux from the outer regions may be causing the Bregman *et al.* broad beam ratio to be lower than our value obtained in the central 10″.

The temperature distribution is peaked in the center of the nebula, decreasing gradually toward the ring. There are two regions of relatively low temperature, located to the north and south of the central peak, rotated approximately 60° from the emission peaks observed in the IR and radio maps. Assuming a source model of an ellipsoidal shell (see below), the temperature is lowest in the polar regions of the nebula and

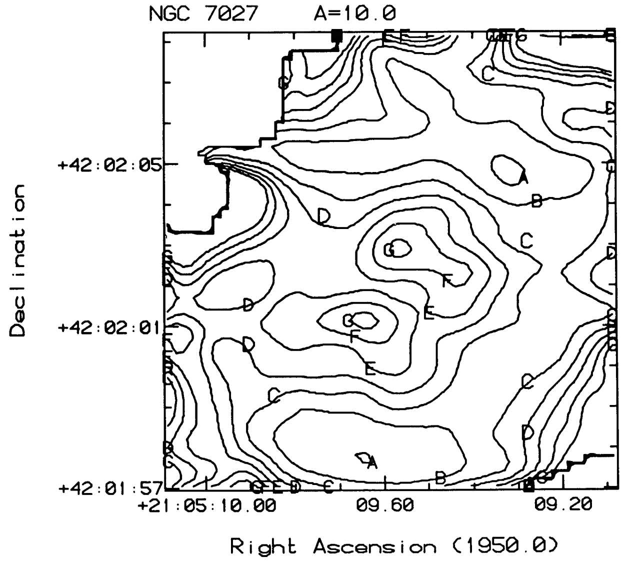

FIG. 10.—The emission temperature map of NGC 7027, calculated from the 3.3 μm data from Woodward (1988) and the 11.2 feature map of Tresch-Fienberg (1985). The temperature is peaked in the center of the nebula, falling off slightly in the ring, with minima to the N and S of the nebula center. The contour level spacing is 20 K, starting from level A = 710 K. The average temperature in the central 10″ is 755 ± 46 K.

highest in the center and equatorial regions which are closer to the source of radiation. The emission temperature derived here is significantly higher than the 90 K temperature derived for the grains with the highest IR luminosity (Natta and Panagia 1981), or the higher temperature (230 K) derived for the dust component responsible for the 10 μm continuum radiation.

One model which would explain these high temperatures is thermal fluctuations of small grains (Sellgren 1984). The heat capacities of these grains are low, so that when one is excited by absorbing a UV photon, it momentarily reaches a high temperature. Since the small grain emits most of its energy at this high temperature (Leger and d'Hendecourt 1987), the observed color temperature will be high. The grain cooling time is much shorter than the time between UV absorptions, so the mean temperature of a grain will be much lower than the peak temperature. The mean temperature of the small grains would be similar to the grains that are responsible for the 90 K emission, which are thought to be larger grains where temperature fluctuations are negligible.

The identification of the UIR features as emission from PAH molecules is not complete. There are still many aspects of the observations that are not well accounted for. This is in part due to lack of laboratory data of these molecules in astronomical conditions. Also, no one molecule or family of molecules has been shown to reproduce all the UIR bands. In particular, there are problems with reproducing the 7.7 and 11.3 μm UIR features in lab spectra of specific PAH molecules. However, the data presented here are consistent with the general aspects of the PAH model in that the UIR feature emission at 7.7 and 11.3 μm is spatially correlated, providing evidence that one species of emitters is responsible for the UIR feature emission. This is also supported by the correlation studies by Cohen *et al.* (1986) discussed above. Identifying the molecule or family of molecules responsible for the UIR emission, however, will require more laboratory investigations into these or other possible models.

g) Source Morphology

The simplest morphological structure of a planetary nebula would be a spherical shell of material expanding uniformly away from the central star. The appearance of most nebulae, however, makes it obvious that the detailed structure of a planetary nebula is much more complex (see the CCD survey by Balick 1987). Nevertheless, the main structure of a planetary nebula can be modeled by a simple geometrical form, such as a thin spheroidal shell. A spherical shell source would give rise to a ring of emission due to limb brightening from our line of sight. In many nebulae, however, the amount of limb brightening observed is greater than would be expected for a shell of uniform thickness and density. In the planetary nebulae presented here, a prominent symmetric, double-lobed structure is observed in addition to a ring of emission. Any model of the source structure must be able to explain these observed features.

There have been many models proposed to account for these observed characteristics. Scott (1973) showed that the 15 GHz radio structure of NGC 7027, which is very similar to the IR and to other radio observations, could be produced by a uniform cylindrical shell of emission, inclined slightly toward the observer. Bentley *et al.* (1984) showed that a similar model fit their IR observations of BD +30°3639. The inclination of the cylinder determines the overall elliptical structure, the lobes are a result of limb brightening in the line of sight passing through the walls of the cylinder, and the central depression is due to the hollow center of the shell. Another model that has been proposed is a prolate ellipsoidal shell (Atherton *et al.* 1979; Balick, Preston, and Icke 1987, Masson 1989*a*, *b*, 1990). In this model, the observed overall shape is determined by the major to minor axis ratio and the inclination of the shell toward the observer. The bipolar structure is aligned along the minor axis of the ellipsoid. The lobes of emission are a result of limb brightening and an actual higher emission due to an increased density of material in the equatorial region, from a higher mass-loss rate (Balick, Preston, and Icke 1987) or a radial dependence of density and radiation from the central star (Masson 1990). The planetary nebulae images presented here provide additional data with which to evaluate these models.

In order to investigate different source models, computer programs were written to display the models and simulated "observations" of the models. A diagram of the cylindrical model used is shown in Figure 11. These models assume that the object is optically thin and calculate the intensity at a particular location on the map by adding up the contribution to the emission from each part of the object along a particular line of sight. This gives a map of the three-dimensional object projected against the two-dimensional plane of the sky. Then, in order to simulate the observation, this projection is convolved with our measured beam profile, to give the map we would expect to observe (with no noise), given the three-dimensional distribution of material in the model.

The simulated observations of a cylindrical model which closely reproduces the observed characteristics of BD +30°3639 is shown in Figure 12. A 10% sinusoidal asymmetry has been added to the uniform cylinder, with the minimum in the western lobe and the maximum in the eastern lobe. This asymmetry reproduces the structure seen in some of the IR maps of BD +30°3639. The model reproduces many of the observed features, such as the double-lobed structure with central minimum, and an underlying ring of emission. The

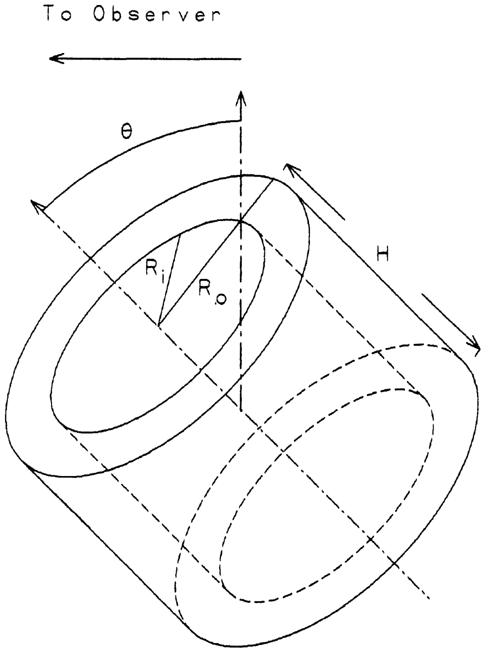

FIG. 11.—Model of planetary nebula used in source simulation. The inner and outer radius (R_i and R_o), height (H), and viewing angle (θ) are shown.

object intensity profile, which rises very steeply near the outside of each lobe and then falls away more slowly toward the central minimum, is also well reproduced. This simple model does not produce any of the bright clumps of emission seen in many of the images (see Fig. 2), but reproduces the general structure of the nebula. The cylindrical model fits the observations of NGC 6572 much closer, since the structure is simpler. The result of this simulation is shown in Figure 13.

Another possible source structure is an ellipsoidal shell. The projection of this type of object would be a limb-brightened ellipse, so some enhancement of emission must take place in the shell to produce the two bright symmetrical lobes of emission observed. Models of this type have been proposed by Atherton *et al.* (1979), and more recently by Balick, Preston, and Icke (1987) and Masson (1990), based on optical and radio observations of a number of planetary nebulae.

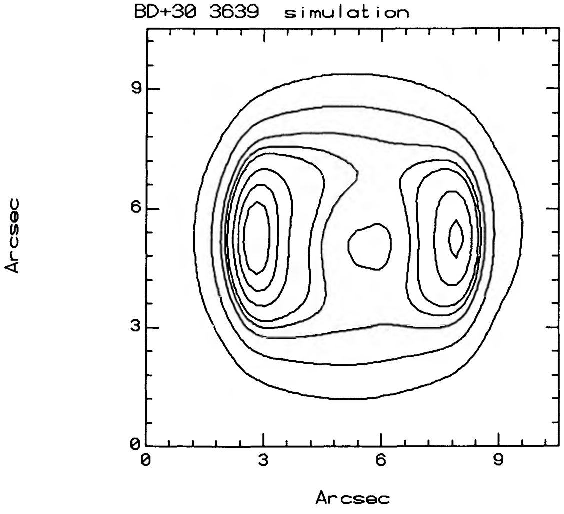

FIG. 12.—The simulated observation of a cylinder ($R_i = 2.''6$, $R_o = 3.''0$, $H = 5.''0$, and viewing angle of 60°) whose characteristics closely resemble the real observations of BD +30°3639.

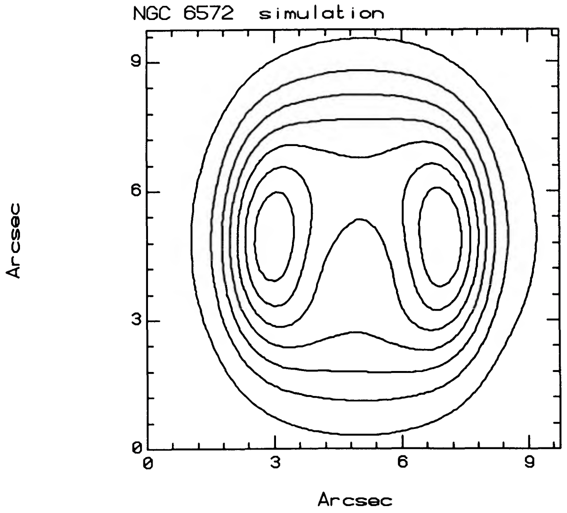

FIG. 13.—The simulated observation of a cylinder ($R_i = 2.''4$, $R_o = 2.''7$, $H = 5.''0$ and viewing angle of 40°) whose characteristics closely resemble the real observations of NGC 6572.

Note that if the equatorial density enhancement of the ellipsoid is high, this structure can be approximated by a cylinder. The cylinder would represent the equatorial regions, and the end caps of the prolate ellipsoidal would be ignored, since the relative intensity of emission would be much lower in those regions. The cylinder model and the ellipsoidal model are therefore roughly equivalent and provide an explanation of how a cylindrical structure might arise.

As noted previously, in BD +30°3639 the radio peaks are rotated 90° with respect to the IR peaks. One possible explanation is that the IR emission is brighter in the polar regions of the ellipsoid, the polar regions being those at the ends of the major axis of the ellipsoid. Masson (1989*b*) has pointed out that since his model accounts for the extreme limb-brightening by viewing the nebulae almost along the major axis, the apparent center of the nebula is actually the part of the ellipsoid farthest from the central star. This implies that since this region has been observed to have the highest temperature in some planetary nebulae, the poles of the ellipsoid may be hotter than the equatorial region. This higher temperature may cause the more intense dust emission in these regions, explaining the difference between the radio and IR emission peaks observed in BD +30°3639.

A bright polar region model, however, does not reproduce the IR observations as well as the ellipsoidal shell with bright equatorial regions. The result of this simulation is shown in Figure 14. The model reproduces some of the structure of BD +30°3639 in the mid-infrared, such as the symmetrical lobes of emission and elliptical form, but the bright ring and central depression as seen in BD +30°3639 cannot be easily produced by this model. Also, this model was calculated for the line of sight directly through the equator of the nebula, perpendicular to the polar axis. This simulates the observed IR structure of the lobes of emission located at the extreme edge of the nebula. However, if the major axis of the nebula differs from the line of sight, these lobes would be located in projection much closer to the center of the nebula, filling up the central minimum. The bright lobes of emission seem to be located at the extreme edge of the IR nebula, since the peak and source size of the IR

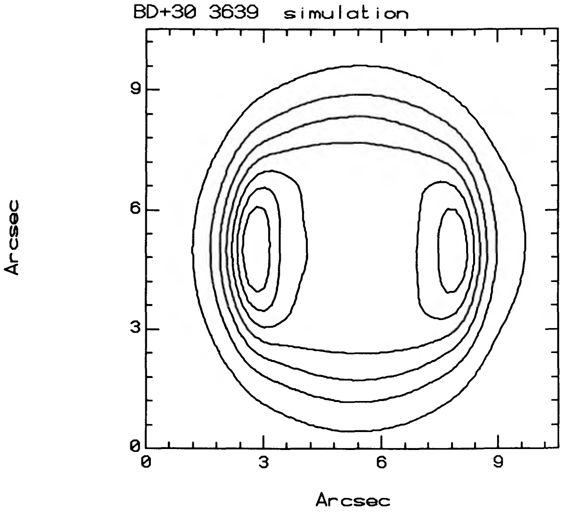

FIG. 14.—Observations of a spherical shell ($R_i = 2.8$, $R_o = 3.0$) with bright polar regions, whose characteristics were chosen to resemble the real observations of BD +30°3639.

emission is as large or greater than the extent of the radio emission in that direction.

Both these models for BD +30°3639, the ellipsoidal shell with either equatorial or polar enhanced IR emission, reproduce the bipolar, elliptical structure observed in the planetary nebula. The model of enhanced emission in the polar regions of the ellipsoid, however, does not fit the data as well as the model of enhanced equatorial emission. In NGC 7027, the enhancement occurs along what appears to be the minor axis of the ellipsoid, coincident with the radio emission. The model does not explain the different radio and IR structure observed in BD +30°3639 either, as described above. Neither model explains why the relationship between the radio and IR emission in BD +30°3639 should be different than the emission in NGC 7027 and NGC 6572, when the nebulae are so similar in many other respects.

By comparing the infrared images presented here to simulated observations of various model sources, we see that the observed structures in NGC 7027 and NGC 6572 are consistent with an ellipsoidal shell model of the source or a cylindrical shell of emission. A cylindrical distribution could be the result of an increased equatorial emission due to either a higher temperature region at the equator or a higher dust density region. The nebula BD +30°3639 does not fit as well into these simple models, and the structure cannot be easily explained by a higher polar emission. The clumping of the IR emission in BD +30°3639, especially in the 12.4 μm map (see Fig. 2), may indicate that the distribution cannot be well modeled by a uniform shell.

IV. CONCLUSIONS

Two planetary nebulae, BD +30°3639 and NGC 6572, have been observed at high resolution (0″.78 per pixel) in five mid-IR wavelengths with a 10 μm CID camera. Calibrated isophotal intensity maps of the planetary nebulae are presented, along with ratio maps, UIR feature maps, temperature maps, and earlier maps of NGC 7027. The IR maps of these nebulae are compared to VLA maps of similar resolution. The following conclusions can be drawn:

1. The observations of the planetary nebulae BD +30°3639 and NGC 6572 show that they exhibit the same general source structure (double-lobed, elliptical with central minimum) as was previously observed in NGC 7027. The nebula BD +30°3639, with a ratio of $C/O \gg 1$, has UIR feature emission at 7.7, 8.6, and 11.3 μm, whereas NGC 6572, with $C/O \approx 1$, has weak feature emission at these wavelengths.

The spatial distribution of the feature emission in BD +30°3639 provides evidence for at least two populations of emitting grains, one responsible for the continuum emission and the other producing the feature emission in the UIR bands. The continuum emission, in general, is more centrally located in the nebula than the feature emission. There are bright lobes of feature emission in the nebulae which are not present or much dimmer at continuum wavelengths. This is similar to previous results for NGC 7027.

In NGC 6572, the spatial distribution of the emission indicates that 11.3 μm feature emission is seen, and it also provides evidence for feature emission at 8.6 μm.

2. The correspondence between the radio maps of BD +30°3639 and NGC 6572 and the IR maps at similar resolution was high, providing evidence that the gas and dust are coextensive. This is similar to the results for NGC 7027 found by Tresch-Fienberg *et al.* (1987). The planetary nebula BD +30°3639 is the exception to this, with the IR lobes located 90° apart from the radio lobes. The emission in the UIR feature maps is slightly more extended than in the radio and IR continuum maps, suggesting that the region of feature emission is on the outer edge of the IR continuum emission region.

3. The spatial correlation between the UIR features in the nebulae BD +30°3639 and NGC 7027 are consistent with models of emission with a single molecule or family of molecules (such as PAHs) responsible for the emission features. The spatial distribution of the 11.2 μm emission in NGC 6572 cannot be easily accounted for solely by SiC emission, and it provides evidence for the presence of emission in the 11.3 μm UIR feature. The detection of spectral features through their spatial distinctness is a unique capability of imaging with arrays.

4. The observed source structure of these planetary nebulae was found to be consistent with a cylindrical shell model or an ellipsoidal shell model with high equatorial emission. The model with bright IR emission in the polar regions of an ellipsoid does not fit the data as well. The clumpy IR structure of BD +30°3639, however, indicates that the actual structure of the nebula is more complex than a symmetrical uniform shell of emission.

We would like to thank C. R. Masson for making his VLA images of the nebulae available to us, and C. E. Woodward for providing the BD +30°3639 3.3 μm map. We also thank J. Black, R. Wade, and M. Rieke for helpful comments and suggestions during the preparation of this paper.

REFERENCES

Aitken, D. K. 1981, in *IAU Symposium 96, Infrared Astronomy*, ed. C. G. Wynn-Williams and D. P. Cruikshank (Dordrecht: Reidel), p. 207.
Aitken, D. K., and Roche, P. F. 1982, *M.N.R.A.S.*, **200**, 217.
———. 1983, *M.N.R.A.S.*, **202**, 1233.
Allamandola, L. J., Greenberg, J. M., and Norman, C. A. 1979, *Astr. Ap.*, **77**, 66.
Allamandola, L. J., Tielens, A. G. G. M., and Barker, J. R. 1985, *Ap. J.* (*Letters*), **290**, L25.
Arens, J. F., Lamb, G. M., and Peck, M. C. 1981, *Proc. SPIE*, **280**, 61.
———. 1983, *Opt. Engineering*, **22**, 267.
Arens, J. F., Lamb, G. M., Peck, M. C., Moseley, H., Hoffmann, W. F., Tresch-Fienberg, R. M., and Fazio, G. G. 1984, *Ap. J.*, **279**, 685.
Atherton, P. D., Hicks, T. R., Reay, N. K., Robinson, G. J., Worswick, S. P., and Phillips, J. P. 1979, *Ap. J.*, **232**, 786.
Atherton, P. D., Hicks, T. R., Reay, N. K., Worswick, S. P., and Hayden Smith, W. 1978, *Astr. Ap.*, **66**, 297.
Balick, B. 1987, *A.J.*, **94**, 671.
Balick, B., Preston, H. L., and Icke, V. 1987, *A.J.*, **94**, 1641.
Barlow, M. J. 1983, in *IAU Symposium 103, Planetary Nebulae*, ed. D. R. Flower (Dordrecht: Reidel), p. 105.
Barnea, D. I., and Silverman, H. F. 1972, *IEEE Trans. Comput.*, **C-21**, 179.
Basart, J. P., and Daub, C. T. 1987, *Ap. J.*, **317**, 412.
Bentley, A. F. 1982, *A.J.*, **87**, 1810.
Bentley, A. F., Hackwell, J. A., Grasdalen, G. L., and Gehrz, R. D. 1984, *Ap. J.*, **278**, 665.
Bregman, J. D., Dinerstein, H. L., Goebel, J. H., Lester, D. E., Witteborn, F. C., and Rank, D. M. 1983, *Ap. J.*, **274**, 666.
Cohen, M., Allamandola, L., Tielens, A. G. G. M., Bregman, J., Simpson, J. P., Witteborn, F. C., Wooden, D., and Rank, D. 1986, *Ap. J.*, **302**, 737.
Curtis, H. D. 1918, *Pub. Lick Obs.*, **13**, 55.
de Muison, M., d'Hendecourt, L. B., and Geballe, T. R. 1987, in *Polycyclic Aromatic Hydrocarbons and Astrophysics*, ed. A. Leger, L. d'Hendecourt, and N. Boccara (Dordrecht: Reidel), p. 287.
d'Hendecourt, L. B., and Leger, A. 1987, in *Planetary and Protoplanetary Nebulae: From IRAS to ISO*, ed. A. Preite Martinez (Dordrecht: Reidel), p. 203.
Duley, W. W. 1985, *M.N.R.A.S.*, **215**, 259.
Duley, W. W., and Williams, D. A. 1981, *M.N.R.A.S.*, **196**, 269.
Friedemann, C. 1969, *Physica*, **41**, 139.
Gillett, F. C., Merrill, K. M., and Stein, W. A. 1972, *Ap. J.*, **172**, 367.
Gilman, R. C. 1969, *Ap. J.* (*Letters*), **155**, L185.
Gilra, D. P. 1972, in *Scientific Results from Orbiting Astronomical Observatory* (*OAO-2*), ed. A. Code (NASA SP-310), p. 295.
———. 1973, in *IAU Symposium 52, Interstellar Dust and Related Topics*, ed. J. M. Greenberg and H. C. van de Hulst (Dordrecht: Reidel), p. 517.
Hoffmann, W. F., Fazio, G. G., Tresch-Fienberg, R. M., Deutsch, L. K., Gezari, D. Y., Lamb, G. M., Shu, P. K., and McCreight, C. R. 1987, in *Infrared Astronomy with Arrays*, ed. C. G. Wynn-Williams and E. E. Becklin (Honolulu: University of Hawaii), p. 241.
Jameson, R. F., Longmore, A. J., McLinn, J. A., and Woolf, N. J. 1974, *Ap. J.*, **190**, 353.
Khromov, G. S., and Kohoutek, L. 1968, in *IAU Symposium 34, Planetary Nebulae*, ed. D. E. Osterbrock and C. R. O'Dell (Dordrecht: Reidel), p. 227.
Lamb, G. M., Gezari, D. Y., Shu, P. K., Tresch-Fienberg, R., Fazio, G. G., and Hoffmann, W. F. 1983, in *Proc. Infrared Detector Technology Workshop*, ed. C. R. McCreight (NASA Ames Research Center), p. 13-1.
Lamb, G. M., Gezari, D. Y., Shu, P. K., Tresch-Fienberg, R., Fazio, G. G., Hoffmann, W. F., and McCreight, C. R. 1984, *Proc. SPIE*, **445**, 113.
Leger, A., and d'Hendecourt, L. 1987, in *Polycyclic Aromatic Hydrocarbons and Astrophysics*, ed. A. Leger, L. d'Hendecourt, and N. Boccara (Dordrecht: Reidel), p. 223.
Leger, A., d'Hendecourt, L., and Defourneau, L. 1989, *Astr. Ap.*, **216**, 148.
Leger, A., and Puget, J. L. 1984, *Astr. Ap.*, **137**, L5.
Martin, W. 1987, *Astr. Ap.*, **182**, 290.
Masson, C. R. 1989*a*, *Ap. J.*, **336**, 294.
———. 1989*b*, *Ap. J.*, **346**, 243.
———. 1990, *Ap. J.*, **348**, 580.
Merrill, K. M., Soifer, B. T., and Russell, R. W. 1975, *Ap. J.* (*Letters*), **200**, L37.
Natta, A., and Panagia, N. 1981, *Ap. J.*, **249**, 189.
Olnon, F. M., and Raimond, E. 1986, *Astr. Ap. Suppl.*, **65**, 607.
Phillips, J. P., and Reay, N. K. 1977, *Astr. Ap.*, **59**, 91.
Pottasch, S. R. 1987, in *Planetary and Protoplanetary Nebulae: From IRAS to ISO*, ed. A. Preite Martinez (Dordrecht: Reidel), p. 1.
Puget, J. L., and Leger, A. 1989, *Ann. Rev. Astr. Ap.*, **27**, 161.
Roche, P. F. 1987, in *Planetary and Protoplanetary Nebulae: From IRAS to ISO*, ed. A. Preite Martinez (Dordrecht: Reidel), p. 45.
Russell, R. W., Soifer, B. T., and Merrill, K. M. 1977, *Ap. J.*, **213**, 66.
Russell, R. W., Soifer, B. T., and Willner, S. P. 1977, *Ap. J.* (*Letters*), **217**, L149.
Sakata, A., Wada, S., Onaka, T., and Tokunaga, A. 1987, *Ap. J.* (*Letters*), **320**, L63.
Scott, P. F. 1973, *M.N.R.A.S.*, **161**, 35.
Seaton, M. J. 1983, in *IAU Symposium 103, Planetary Nebulae*, ed. D. R. Flower (Dordrecht: Reidel), p. 129.
Sellgren, K. 1984, *Ap. J.*, **277**, 623.
Shields, G. A. 1978, *Ap. J.*, **219**, 565.
Skilling, J., and Bryan, R. K. 1984, *M.N.R.A.S.*, **211**, 111.
Terzian, Y. 1987, *Sky and Tel.*, **73**, 128.
Torres-Peimbert, S., and Pena, M. 1981, *Rev. Mexicana Astr. Af.*, **6**, 301.
Treffers, R., and Cohen, M. 1974, *Ap. J.*, **188**, 545.
Tresch-Fienberg, R. M. 1985, Ph.D. thesis, Harvard College.
Tresch-Fienberg, R. M., Fazio, G. G., Gezari, D. Y., Hoffmann, W. F., Lamb, G. M., Shu, P. K., and McCreight, C. R. 1987, *Ap. J.*, **312**, 542.
Weir, N. 1987, B.A. thesis, Harvard College.
Willner, S. P. 1982, in *Galactic and Extragalactic IR Spectroscopy*, ed. M. F. Kessler and J. P. Phillips (Dordrecht: Reidel), p. 37.
Willner, S. P., Jones, B., Puetter, R. C., Russell, R. W., and Soifer, B. T. 1979, *Ap. J.*, **234**, 496.
Witteborn, F. C., Sandford, S. A., Bregman, J. D., Allamandola, L. J., Cohen, M., Wooden, D. H., and Graps, A. L. 1989, *Ap. J.*, **341**, 270.
Woodward, C. 1988, Ph. D. thesis, University of Wyoming.
Woodward, C. E., Pipher, J. L., Shure, M. A., Forrest, W. J., Sellgren, K., and Nagata, T. 1987, in *Infrared Astronomy with Arrays*, ed. C. G. Wynn-Williams and E. E. Becklin (Honolulu: University of Hawaii), p. 299.

LYNNE K. DEUTSCH and GIOVANNI G. FAZIO: Harvard-Smithsonian Center for Astrophysics, Mail Stop 65, 60 Garden Street, Cambridge, MA 02138

WILLIAM F. HOFFMANN and JOSEPH L. HORA: Steward Observatory, University of Arizona, Tucson, AZ 85721